CrystEngComm

Solvates of a dianisyl-substituted donor–acceptor-type benzothiadiazole: mechanochromic, vapochromic, and acid-responsive multicolor luminescence

Journal:	*CrystEngComm*
Manuscript ID	CE-ART-12-2022-001705.R1
Article Type:	Paper
Date Submitted by the Author:	08-Mar-2023
Complete List of Authors:	Yagi, Takumi; Yokohama National University, Department of Chemistry and Life Science, Graduate School of Engineering Science Tachikawa, Takashi; Graduate School of Science, Kobe University, Department of Chemistry Ito, Suguru; Yokohama National University, Department of Chemistry and Life Science, Graduate School of Engineering Science

ARTICLE

Solvates of a dianisyl-substituted donor–acceptor-type benzothiadiazole: mechanochromic, vapochromic, and acid-responsive multicolor luminescence

Received 00th January 20xx,
Accepted 00th January 20xx

DOI: 10.1039/x0xx00000x

Takumi Yagi,[a] Takashi Tachikawa[b,c] and Suguru Ito*[a,d]

Recently, great advances have been made in the mechanochromic luminescence (MCL) of organic crystals that can switch their emission colors upon exposure to the mechanical stimuli. Although several polymorphic crystals and solvates have exhibited multicolor MCL properties, a further deep understanding of the relationship between crystal structures and stimuli-responsive properties is required for rationally generating multicolor-emissive polymorphic crystals and solvates from a single luminescent compound. Herein, multicolor luminescence switching has been achieved for solvates of a phenanthroimidazolylbenzothiadiazole derivative with dianisyl groups. Four types of solvates with different luminescence properties changed their emission colors upon amorphization induced by mechanical stimuli. The amorphous state was recrystallized into solvates when exposed to solvent vapors. Furthermore, the solvate containing pyridine molecules showed a bathochromic shift in emission wavelength upon exposure to acid vapor. Typical acid-responsive luminescence switching is characterized by the protonation of the basic moiety of luminescent molecules, whereas in this study, the change in luminescence color could be induced by protonating non-luminescent pyridine molecules in the solvate. The present study potentially provides useful insights for the development of smart luminescent sensors.

Introduction

Luminescent organic crystals with stimuli-responsive properties have recently attracted increasing interest owing to their wide potential applications, especially in sensors and security technologies.[1] Mechanical stimuli such as grinding, shearing, and pressing often induce the switching in emission colors of the crystalline compounds, and the mechanically switched colors typically recover to the original after being heated or exposed to solvents.[2] The mechanism of such mechanochromic luminescence (MCL) is typically based on the amorphization of crystal structures upon grinding followed by recrystallization triggered by a second external stimulus. Consequently, a clear majority of MCL crystals switch the emission color between two colors. Crystals with multicolor MCL properties are attractive from the perspective of a deep understanding of MCL and their application to precise stimuli sensing.[3]

Preparation of polymorphic crystals and solvent-containing crystals (solvates) is promising strategy to achieve multicolor MCL by a single luminescent compound.[4] Since the luminescence color of organic crystals depends on molecular conformation and intermolecular interactions as well as molecular structure, polymorphic crystals and solvates of a luminescent compound may exhibit different emission colors and MCL properties reflecting their molecular arrangements. Although an increasing number of polymorphic crystals and solvates have been reported to show multicolor MCL, little is known about luminescent organic molecules that can form more than two MCL solvates with distinct molecular arrangements.[5]

We have recently reported the versatile MCL behaviors of donor–acceptor (D–A)-type benzothiadiazole derivatives.[6] The molecular design is based on the direct substitution of an electron-donating heteroaromatic ring on the electron-accepting benzothiadiazole ring. Such D–A-type molecules can switch their luminescence properties in response to changes in the dihedral angles between heteroaromatic rings and the polarity of the surrounding environment.[6h] When triphenylimidazole was introduced as the donor moiety, multicolor MCL behaviors were observed by forming solvates with different emission colors.[6d,g] Meanwhile, no solvates were obtained for a series of phenanthroimidazole-substituted derivatives.[6e,h]

Herein, we report multicolor MCL of solvates of phenanthroimidazolylbenzothiadiazole **1** bearing dianisyl

[a] Department of Chemistry and Life Science, Graduate School of Engineering Science, Yokohama National University, 79-5 Tokiwadai, Hodogaya-ku, Yokohama 240-8501, Japan. E-mail: suguru-ito@ynu.ac.jp
[b] Department of Chemistry, Graduate School of Science, Kobe University, 1-1 Rokkodai-cho, Nada-ku, Kobe 657-8501, Japan
[c] Molecular Photoscience Research Center, Kobe University, 1-1 Rokkodai-cho, Nada-ku, Kobe 657-8501, Japan
[d] PRESTO, Japan Science and Technology Agency (JST), 4-1-8 Honcho, Kawaguchi, Saitama 332-0012, Japan

† Electronic Supplementary Information (ESI) available: Supplementary fluorescence and absorption spectra, single-crystal X-ray diffraction analyses, theoretical calculations, PXRD data, and NMR spectra. CCDC 2232778 (**1•Toluene**), 2232779 (**1•CHCl$_3$**), 2232780 (**1•Benzene**), 2232781 (**1•Pyridine**), 2232782 (**1•EtOAc**), and 2232783 (**1**). See DOI: 10.1039/x0xx00000x

groups (Fig. 1a). Five solvent-containing and one solvent-free crystals of **1** with MCL properties were obtained, and the molecular arrangements of **1** in these crystals were classified into four types. In contrast to the previous mechano-responsive solvates,[6g] solvent-containing crystals were recrystallized upon exposing ground amorphous **1** to solvent vapors. Furthermore, pyridine-containing solvate **1•Pyridine** exhibited acid vapor-responsive luminescence switching. The usual acid-responsive luminescence switching involves the protonation of a basic moiety in a luminescent molecule (Fig. 1b).[7] In the present method, the emission-color change is attributed to the protonation of the non-luminescent basic solvent in the solvate, which provides a unique approach to acid-responsive luminescence.

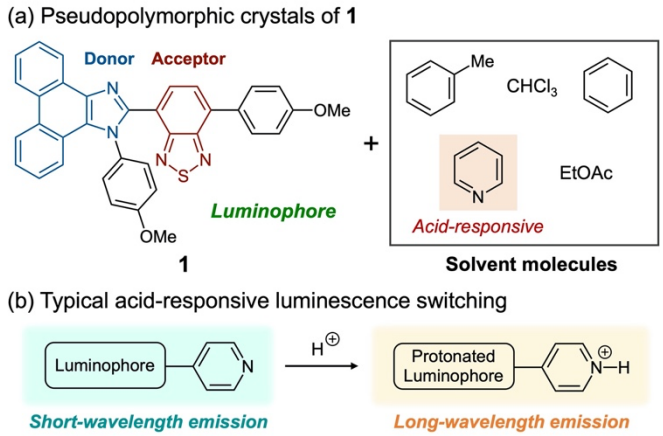

Fig. 1 (a) Structure of **1** and solvent molecules used in forming solvates. (b) Typical mechanism for the acid-responsive luminescence switching.

Results and discussion

Synthesis and emission properties

Following a previously reported procedure for the synthesis of diphenyl-substituted derivative,[6h] dianisyl-substituted phenanthroimidazolylbenzothiadiazole **1** was synthesized by a four-component condensation followed by a Suzuki–Miyaura coupling reaction (Scheme 1). A mixture of 9,10-phenanthrenequinone, ammonium acetate (5.0 equiv.), *p*-anisidine (1.5 equiv.), and 4-bromo-7-formyl-2,1,3-benzothiadiazole (1.0 equiv.) was refluxed in toluene for 16 h in the presence of anhydrous sodium sulfate (2.8 equiv.) to afford bromide **2** in 70% yield. The reaction of **2** and 4-methoxyphenylboronic acid (1.3 equiv.) in refluxing toluene/aqueous K_2CO_3 (1.4 M) for 14 h in the presence of $Pd(PPh_3)_4$ (4 mol%) gave **1** in 86% yield.

When **1** was recrystallized from various solvents, it was found that **1** is prone to form solvates containing solvent molecules in the crystal lattice. Recrystallization of **1** from toluene afforded solvate **1•Toluene** that contain toluene molecules. These crystals showed yellow emission with a maximum fluorescence wavelength (λ_{em}) of 565 nm and a high fluorescence quantum yield (Φ_F) of 0.76 (Fig. 2). The ^{1}H NMR spectrum of **1•Toluene** indicated that the solvate consist of an equimolar amount of **1** and toluene molecules. Furthermore, the crystallization of **1** from various solvents (chloroform, benzene, pyridine, and ethyl acetate) gave the corresponding solvates. Chloroform-containing crystals **1•CHCl$_3$** showed green emission (λ_{em} = 508 nm, Φ_F = 0.67), whereas **1•Benzene**, **1•Pyridine**, and **1•EtOAc** containing benzene, pyridine, and ethyl acetate, respectively, exhibited yellow-green emission (λ_{em} = 521–524 nm, Φ_F = 0.74–0.83). Yellow-emissive crystals of **1** without solvates were obtained by crystallization from *tert*-butylbenzene (λ_{em} = 550 nm, Φ_F = 0.71). One reason for the absence of *tert*-butylbenzene in the crystal structure would be the high steric bulkiness of the *tert*-butyl group.

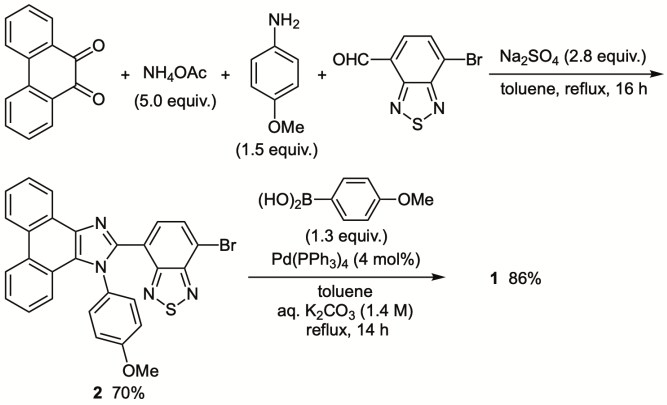

Scheme 1 Synthesis of **1**

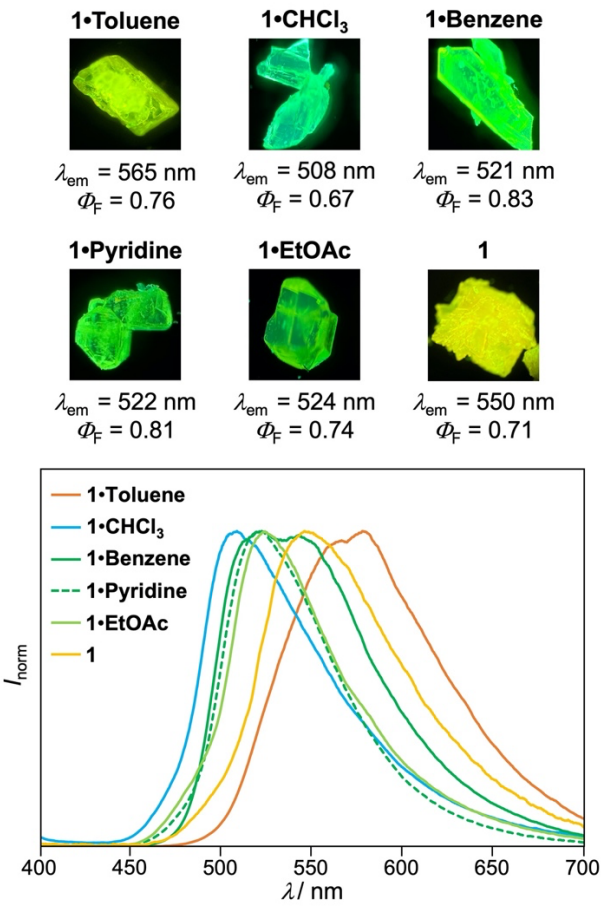

Fig. 2 Photographs and fluorescence spectra of solvates **1•Solvent** and crystalline **1** under UV (365 nm) irradiation.

The emission wavelengths of crystalline **1** containing solvate molecules were significantly different from those of solutions in the corresponding solvent. Typical solvatofluorochromism, characteristic to donor–acceptor-type fluorophores, was observed for **1** in organic solvents with different polarities (Fig. S1). For example, a less polar toluene solution of **1** exhibited green emission (λ_{em} = 550 nm, Φ_F = 0.77), whereas orange emission was observed from a polar pyridine solution of **1** (λ_{em} = 582 nm, Φ_F = 0.50).

Crystal structures

Single-crystal X-ray structure analyses of **1** and its solvates were performed to elucidate the relationship between luminescence color and crystal structure (Fig. 3, Fig. S2–S6 and Table S1). In all solvates, two molecules in close proximity formed intermolecular π-stacks between anisyl groups on the nitrogen atom at a distance of 3.223–3.409 Å. The methoxy groups of the stacked anisyl groups formed CH–π interactions with the other benzothiadiazole ring (2.542–2.658 Å) (Fig. 3a left and Fig. S2–S5).

Both **1•Benzene** and **1•Pyridine** are monoclinic with the same space group *C*2/*c*, and the solvent molecules were contained in one-dimensional channel structures (Fig. 3a right and Fig. S3). The molar ratio of **1** to solvate molecules was 1:1, as suggested by their ^{1}H NMR spectra. Crystals of **1•Toluene** in the triclinic *P*-1 space group also formed one-dimensional channel structures, which were filled with toluene molecules (**1**/toluene = 1:1) (Fig. 3b).

In contrast, both **1•CHCl$_3$** and **1•EtOAc** are monoclinic crystals with the same space group $P2_1/c$. Two isolated chloroform molecules in **1•CHCl$_3$** were surrounded by adjacent **1** molecules (Fig. 3c). Similarly, ethyl acetate molecules should be present in **1•EtOAc** at the voids where chloroform molecules were contained in **1•CHCl$_3$**, although the disordered solvent molecules of **1•EtOAc** were removed by the SQUEEZE method

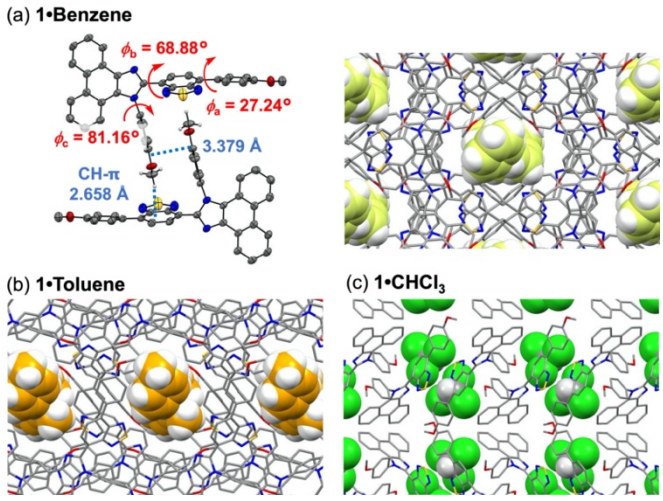

Fig. 3 Crystal structures of (a) **1•Benzene**, (b) **1•Toluene**, and (c) **1•CHCl$_3$**. Solvate molecules are represented with space-filling model. Color code: gray = C; red = O; blue = N; yellow = S.

(Fig. S4).[8] The ^{1}H NMR spectra indicated the molar ratios of **1** to solvate molecules were 1:1 and 1:0.5 for **1•CHCl$_3$** and **1•EtOAc**, respectively.

On the other hand, the single crystal consisting only of **1** is triclinic with the space group *P*-1, which is composed of four crystallographically independent molecules (Fig. S6). Contrary to the solvates, the anisyl groups did not form intermolecular stacks or CH–π interactions with benzothiadiazole rings. Alternatively, intermolecular π-stacks were observed between phenanthroimidazole rings.

Based on the single-crystal X-ray structure analyses, we compared the emission color and molecular conformation of crystalline **1** and its solvates. In the previous report,[6h] we proposed that the emission wavelength of phenanthroimidazolylbenzothiadiazole derivatives is dictated by the dihedral angles of adjacent (hetero)aryl rings. The dihedral angles between the *C*-anisyl and the benzothiadiazole rings (ϕ_a), between the benzothiadiazole and the phenanthroimidazole rings (ϕ_b), and between the phenanthroimidazole and the *N*-anisyl rings (ϕ_c) are summarized in Table 1. Since the absorption spectra of the crystalline samples are broad and the maxima are unclear (Fig. S7), Table 1 compares the experimental emission maxima of the crystals to the calculated absorption wavelengths of the molecules in the crystalline state (λ_{abs}). The theoretical λ_{abs} values were calculated based on the time-dependent density functional theory (TD-DFT) at the CAM-B3LYP/6-31G(d) level of theory for the single molecular structures obtained from the X-ray diffraction analyses (Table S2 and Fig. S8).

As shown in Fig. 2, **1•Benzene** and **1•Pyridine** exhibited almost identical emission properties regardless of the inclusion of different solvates. The dihedral angles and calculated λ_{abs} values of **1•Benzene** and **1•Pyridine** are comparable (ϕ_a + ϕ_b + ϕ_c: 177.28° for **1•Benzene**, 178.37° for **1•Pyridine**; calcd. λ_{abs}: 379 nm for **1•Benzene**, 377 nm for **1•Pyridine**), indicating that these crystals exhibit almost the same molecular conformation and arrangement of **1**. Since the solvent molecules are present in the one-dimensional channels of **1•Benzene** and **1•Pyridine**, the intermolecular interactions between the solvent molecules and crystalline **1** should be insufficient to affect the emission properties.

The different emission wavelengths exhibited by **1•CHCl$_3$** and **1•EtOAc** should be explained by the molecular conformation of **1** in these solvates. Although both **1•CHCl$_3$** and **1•EtOAc** crystallized in the same space group, **1** in **1•EtOAc** exhibits more planar molecular conformation relative to **1•CHCl$_3$** (ϕ_a + ϕ_b + ϕ_c: 175.29° for **1•EtOAc**, 183.21° for **1•CHCl$_3$**). Accordingly, the calculated λ_{abs} of **1•EtOAc** (381 nm) is larger than that of **1•CHCl$_3$** (373 nm), which should account for the bathochromically shifted emission spectrum of **1•EtOAc** compared with that of **1•CHCl$_3$**.

The emission from **1•Toluene** was observed at a longer wavelength region compared to other solvates, even though the calculated absorption wavelength was comparable to **1•EtOAc**. The powder X-ray diffraction (PXRD) analysis of **1•Toluene** showed intense diffraction peaks originating from the (010) and (020) planes (Fig. S14d). This result suggests the

Table 1. Maximum emission wavelengths (λ_{em}), calculated maximum absorption wavelengths (λ_{abs}), calculated oscillator strengths, dihedral angles (ϕ_a, ϕ_b, and ϕ_c), and sum of the dihedral angles (ϕ_a–ϕ_c) of **1** and its solvates.

	Crystalline λ_{em} (nm)	Calcd λ_{abs} (nm)[a]	Oscillator strength[a]	Dihedral angle (°)[b]			$\phi_a+\phi_b+\phi_c$ (°)
				ϕ_a	ϕ_b	ϕ_c	
1•CHCl₃	508	373	0.390	39.37	64.30	79.54	183.21
1•Benzene	521	379	0.422	27.24	68.88	81.16	177.28
1•Pyridine	522	377	0.408	26.52	69.59	82.26	178.37
1•EtOAc	524	381	0.428	30.29	65.24	79.76	175.29
1•Toluene	565	382	0.471	26.74	56.18	73.14	156.06
1	550	371	0.396	49.76	39.69	87.00	176.45

[a] Time-dependent density functional theory (TD-DFT) calculations were based on their molecular structure in the crystalline state. [b] The dihedral angles (ϕ_a, ϕ_b, and ϕ_c) are the angles between adjacent (hetero)aryl groups.

selective growth along the *a*- and *c*-axes of **1•Toluene**, which caused the self-absorption of fluorescence at the short wavelength region,[9] resulting in the apparent bathochromic shift of the emission spectrum relative to the other polymorphic crystals. Although the reason for the self-absorption caused by the selective growth of *a*- and *c*-axes has not been fully elucidated at this time, one possibility is that the relatively dense stacks of **1** in the *c*-axis direction may have affected the self-absorption because **1•Toluene** crystals form one-dimensional channel structures in the *c*-axis direction.

The calculated λ_{abs} value of **1** in crystalline **1** (371 nm) is comparable to those in solvates. Nevertheless, the emission band of crystalline **1** was observed in the bathochromic region compared with those of solvates except for **1•Toluene**. Since crystalline **1** does not contain solvate molecules, the crystal packing of **1** is denser than that of solvates. Therefore, the excited state of **1** should be more efficiently stabilized by intermolecular interactions, which should account for bathochromically shifted fluorescence.

Mechanochromic luminescence

The mechanoresponsive properties of various solvates were examined by applying mechanical stimuli using an agate pestle (Fig. S9–14). Notably, **1•Benzene** exhibited a tricolor MCL (Fig. 4). Upon grinding, the emission color of crystalline **1•Benzene** bathochromically changed from green to yellow-orange (λ_{em} = 576 nm, Φ_F = 0.81). When the ground state was exposed to benzene vapor, the emission color hypsochromically changed to yellow-green (λ_{em} = 552 nm, Φ_F = 0.70). The yellow-orange-emissive state was recovered by grinding the yellow-green-emissive state.

The PXRD analyses of **1•Benzene** showed that the diffraction peaks decreased by grinding crystalline **1•Benzene**, which indicates the amorphization of the crystal structure (Fig. 5a). The diffraction peaks of crystalline **1•Benzene** were partially recovered after exposing the ground state to benzene vapor. This result suggests that amorphous **1** is recrystallized by incorporating benzene molecules. However, the diffraction intensity of the benzene-exposed state was not fully recovered compared with the initial crystalline state, and the intensity ratio of the diffraction peak after benzene exposure was different from that of the original crystal. Since the crystallinity and crystal habit are different between the initial crystal and the benzene-exposed state, the emission color of the benzene-exposed state is different from that of the initial crystal, probably due to the varying degree of intermolecular interactions.

Differential scanning calorimetry (DSC) measurements were performed for crystalline and ground **1•Benzene** (Fig. 5b). The DSC thermogram of crystalline **1•Benzene** showed an endothermic peak at 130 °C, which originated from the release of benzene molecules from the crystals. Subsequently, another endothermic peak that corresponds to the melting point (T_m) of **1** was observed at 220 °C. For ground **1•Benzene**, an endothermic peak originating from the release of benzene molecules was observed at 119 °C, followed by a crystallization peak (T_c) at 153 °C.

The ^{1}H NMR spectrum showed the presence of benzene molecules in ground **1•Benzene**. The ratio of **1** to benzene was 1:0.5 in the ground state, and most of the benzene molecules remained after vacuum drying of the ground sample (Fig. S15). These results indicate that benzene molecules in the crystal lattice were released by grinding crystalline **1•Benzene**, whereas half of the benzene molecules remained after grinding. As shown in the PXRD analysis, part of crystalline **1•Benzene** remained in the ground state. Accordingly, ground **1•Benzene** should be a mixture of crystalline **1•Benzene** and amorphous **1**, and partial amorphization should be sufficient to induce the emission-color change by grinding.

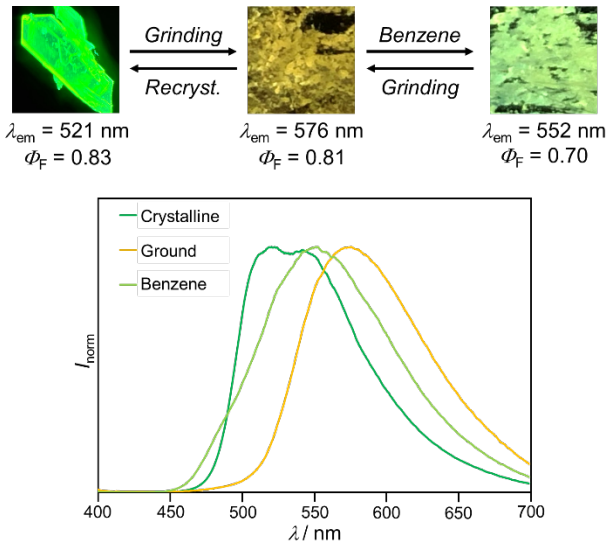

Fig. 4 Photographs and fluorescence spectra for the tricolor MCL of **1•Benzene** excited with UV light (365 nm).

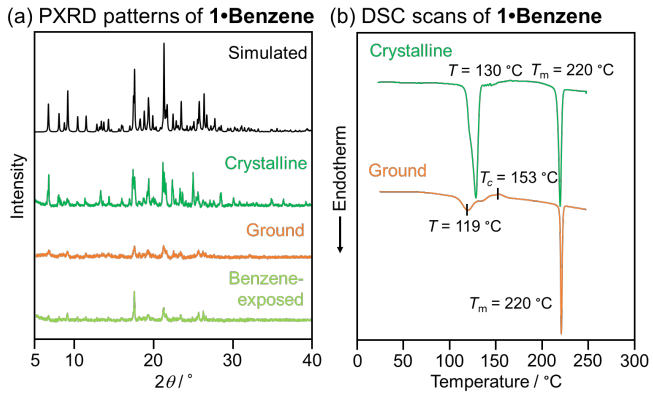

Fig. 5 (a) PXRD patterns of **1•Benzene**. Simulated patterns calculated from the single-crystal X-ray diffraction structures prepared by cooling a hot benzene solution of **1** (black). Experimental patterns of the samples prepared by recrystallization from benzene (green), after grinding (orange), and after being exposed with benzene (yellow-green). (b) DSC scans of **1•Benzene** for the samples prepared by recrystallization from benzene (green) and after grinding (orange).

The emission color of crystalline **1** also changed to yellow-orange after grinding (Fig. 6). When crystalline **1** was crushed into fine powders, the emission color hypsochromically shifted from yellow to yellow-green (λ_{em} = 540 nm). Further grinding induced the bathochromic shift of the emission band to show yellow-orange emission (λ_{em} = 579 nm, Φ_F = 0.69), and the yellow-green-emissive state was restored on heating the yellow-orange-emissive state to 160 °C for 10 min. These results support the hypothesis that the yellow-orange emission from ground **1•Benzene** originated from amorphous **1**.

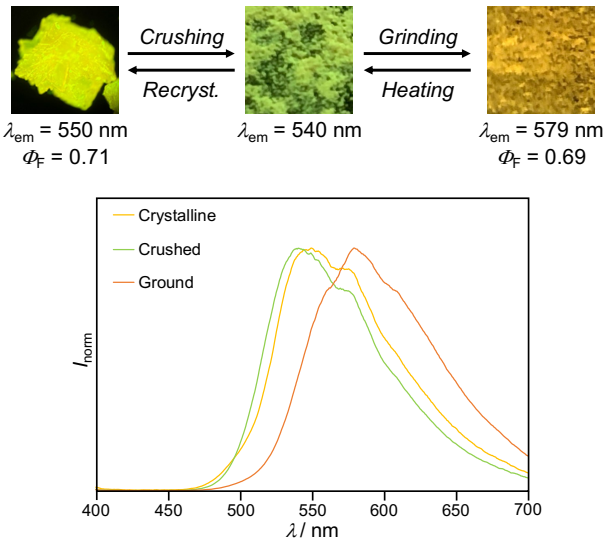

Fig. 6 Photographs and fluorescence spectra for the two-step MCL of **1** excited with UV light (365 nm).

The PXRD analyses of **1** revealed that some intense peaks of crystalline **1** reduced upon crushing, although the crystal structure was retained in the crushed state (Fig. 7a). Accordingly, the hypsochromic shift of the emission band would be rationalized by the reduction of the self-absorption of luminescence for the smaller crushed crystals. The diffraction peaks decreased significantly upon grinding and recovered after heating, indicating the transition between crystalline and amorphous states.

The DSC measurements also supported that the MCL of **1** between yellow-green and yellow-orange emission should be attributed to the crystal-to-amorphous phase transitions (Fig. 7b). In the DSC thermogram of crystalline **1**, the endothermic peak that corresponds to the melting point was observed at 216 °C. On the other hand, a cold-crystallization peak was observed at 110 °C for the DSC thermogram of ground **1**.

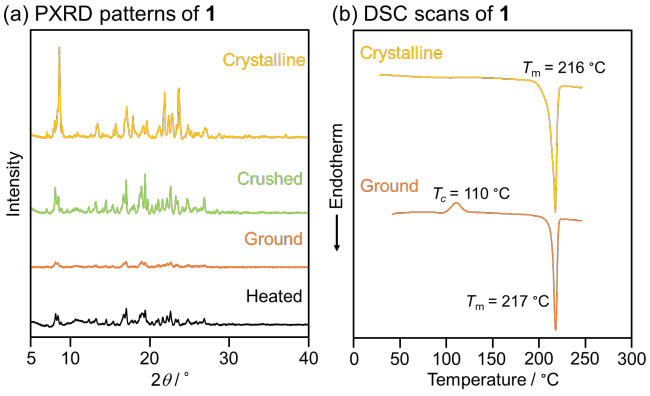

Fig. 7 (a) PXRD patterns of **1**. Experimental patterns of the samples prepared by recrystallization from *tert*-butylbenzene (yellow), after crushing (yellow-green), after griding (orange), and after heating at 160 °C for 10 min (black). (b) DSC scans of **1** for the samples prepared by recrystallization from *tert*-butylbenzene (yellow) and after grinding (orange).

Given that the emission color was changed upon exposing ground **1** to benzene, we investigated the exposure of the ground **1**, prepared from **1•Benzene**, to other solvent vapors (Fig. 8). The emission color changed differently depending on the exposed solvent. Upon exposing ground **1** to chloroform vapor, the emission color changed to blue-green (λ_{em} = 505 nm). This emission color is similar to that of solvate **1•CHCl₃** (λ_{em} = 508 nm), suggesting that the amorphous state recrystallized into **1•CHCl₃**. When ground **1** was exposed to pyridine and ethyl acetate vapor, the emission color changed to yellow-green with λ_{em} at 522 nm and 523 nm, respectively. These emission wavelengths also suggest the formation of solvates **1•Pyridine** and **1•EtOAc**. On the other hand, the emission color changed to yellow-green (λ_{em} = 542 nm) by exposing ground **1** to toluene vapor. This emission color was different from the yellow emission of crystalline **1•Toluene** (λ_{em} = 565 nm) obtained by recrystallization from toluene. Meanwhile, upon crushing yellow-emissive crystalline **1•Toluene**, the emission wavelength hypsochromically shifted to 543 nm probably due to the reduction of the self-absorption (Fig. S13). Since the emission wavelength of the crushed **1•Toluene** is almost identical to that of toluene-exposed **1**, the recrystallization of **1•Toluene** should occur upon exposing ground **1** to toluene vapor. All solvent-exposed states returned to the yellow-orange-emissive amorphous state by grinding.

The PXRD measurements of solvent-exposed **1** showed different diffraction patterns depending on the exposed solvent. Each diffraction pattern was consistent with that of the corresponding solvate (Fig. 9 and Fig. S14). These results suggest that amorphous **1** incorporated the exposed solvent molecules and formed solvates. In the case of **1•Benzene** and **1•Toluene**, the intensity ratios of the diffraction peaks were significantly different between the solvent-exposed states and the bulk crystals obtained from the solutions. These differences

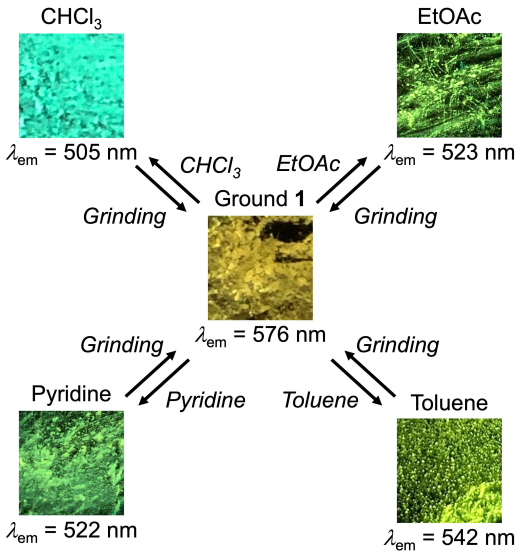

Fig. 8 Photographs for ground **1** (center), chloroform-exposed **1** (top left), pyridine-exposed **1** (bottom left), ethyl acetate-exposed **1** (top right), and toluene-exposed **1** (bottom right) under UV (365 nm) irradiation.

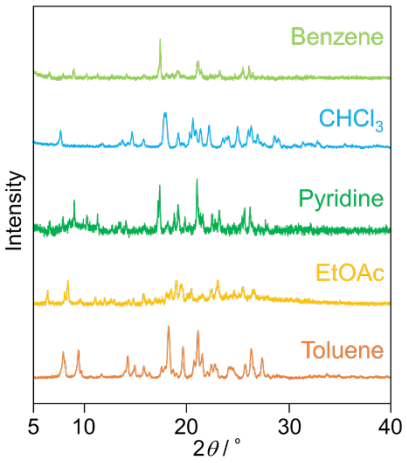

Fig. 9 PXRD patterns of solvent-exposed **1** prepared by exposing ground **1** to solvent vapors (yellow-green = benzene-exposed **1**; blue = chloroform-exposed **1**; green = pyridine-exposed **1**; yellow = ethyl acetate-exposed **1**; orange = toluene-exposed **1**).

in crystallinity should account for their different emission wavelengths.

Acid-responsive luminescence

The acid-responsive behavior of **1•Pyridine** was investigated by exposing to HCl vapor (Fig. 10 and S16). Upon exposure to HCl vapor for 1 h, the emission color of crystalline **1•Pyridine** bathochromically shifted from green (λ_{em} = 525 nm) to orange (λ_{em} = 586 nm). Meanwhile, the crystal of **1** showed no change in emission color after acid exposure (Fig. S17). The X-ray photoelectron spectroscopy (XPS) indicated the presence of protonated pyridines and chloride ions on the surface of **1•Pyridine** after exposure to HCl vapor (Fig. S18). In addition, a mixture of **1** and pyridine hydrochloride exhibited bathochromically shifted orange emission (Fig. S19). Accordingly, the protonation of pyridine molecules should induce the emission-wavelength shift of **1•Pyridine**. A significant increase in absorption around 500–550 nm was observed for the HCl-exposed orange-emissive state (Fig. S20). The intermolecular interactions between **1** and protonated pyridine should decrease the excitation energy, leading to the emission of bathochromically shifted fluorescence.

The PXRD analyses showed that the HCl-exposed state retained the crystallinity, although not completely identical to the initial crystalline state (Fig. S21). When the acid-exposed **1•Pyridine** was crushed, the emission color was returned to the original green (λ_{em} = 523 nm, Fig. 10 and S16). The absorption around 500–550 nm decreased after crushing (Fig. S20). These observations suggest that only partial pyridine molecules near the crystal surface of **1•Pyridine** were protonated in the orange-emissive state. In fact, only the surface luminescence was orange and the interior showed green emission after cutting a protonated crystal with a razor (Fig. S22).

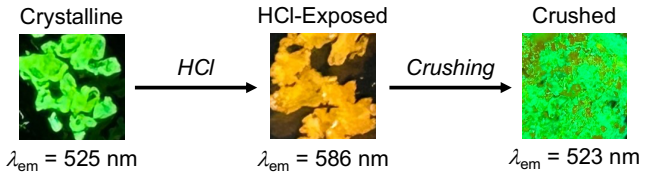

Fig. 10 Photographs of crystalline, HCl-exposed, and crushed **1•Pyridine** under UV (365 nm) irradiation.

Spatially resolved fluorescence microscopy of the acid-exposed crystals revealed that a portion of the crystal surface showed intense green emission, while most of the surface exhibited weak orange emission (Fig. 11a and 11b). Meanwhile, the crushed sample showed mainly intense green emission, with some showing weak orange emission. The fluorescence decay profile of the initial green-emissive crystals fitted well to a single exponential function with a lifetime of 4.5 ns (Fig. 11c and Table 2). After being exposed to HCl vapor, the decay curve fitted well to double exponential functions with significantly decreased lifetimes of 0.24 and 0.98 ns. The decay curve of the crushed sample also fitted well to double exponential functions, and the fluorescence lifetimes of the two components were 1.0 and 3.3 ns. The short-lived component should correspond to the orange-emissive component. Although the long-lived component has a shorter lifetime than green emission from initial crystalline **1**, this can be attributed to an increase in the non-radiative decay process due to partial intermolecular interactions with protonated pyridine molecules.

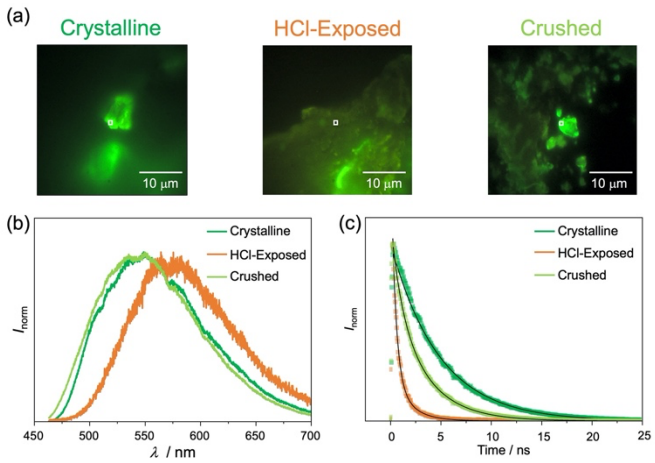

Fig. 11 (a) Photographs, (b) fluorescence spectra, and (c) fluorescence decay profiles of crystalline, HCl-exposed, and crushed **1•Pyridine** recorded at the single-particle level (λ_{ex} = 405 nm). (a) Crystalline (left), HCl-exposed (center), and crushed (right) **1•Pyridine**. The square marks indicate the measured locations of fluorescence spectra and fluorescence decay profiles. (b) Crystalline (green), HCl-exposed (orange), and crushed (yellow-green) **1•Pyridine**. (c) Crystalline (green), HCl-exposed (orange), and crushed (yellow-green) **1•Pyridine**. The black lines indicate single or double exponential curves fitted to the time profiles.

Table 2. Maximum fluorescence wavelengths in the bulk state ($\lambda_{em,bulk}$) and lifetimes (τ) for the three states of **1•Pyridine**

	$\lambda_{em,bulk}$ (nm)[a]	τ_1 (ns)[b]	τ_2 (ns)[b]
Crystalline	525	4.5	–
HCl-Exposed	586	0.24 (0.50)	0.98 (0.50)
Crushed	523	1.0 (0.12)	3.3 (0.88)

[a] The maximum fluorescence wavelength observed in the bulk state (λ_{ex} = 365 nm). [b] The fractional contribution f_n of the component is indicated in parentheses.

Conclusions

In summary, the solvates of dianisyl-substituted phenanthroimidazolylbenzothiadiazoles **1** exhibited different emission colors depending on the molecular conformation, packing structures, and crystallinity rather than on intermolecular interactions between **1** and the solvate molecules. Upon grinding, the emission wavelengths of the solvates shifted in the bathochromic direction to show yellow-orange emission. Exposure of the ground amorphous state to solvent vapors induced the recrystallization of solvates with different emission colors. PXRD measurements showed that the diffraction patterns after exposure to solvents were in good agreement with those of solvates obtained by recrystallization from the corresponding solvents. Moreover, the emission color of **1•Pyridine** changed from green to orange upon exposure to HCl vapor.

The results of this study reinforce the potential of solvates to achieve stimuli-responsive multicolor luminescence from a single luminescent compound. The introduction of *N*-anisyl group in **1** was effective in forming anti-parallel dimers in the crystalline state, which should facilitate the inclusion of solvent molecules between the dimers. Compared to the crystals without solvent molecules, solvates typically show a more prominent change in luminescence colors upon grinding because of the significant increase in intermolecular interactions by amorphization. Protonation of included pyridine molecules provides a new approach for generating acid-responsive crystals, which does not require the direct substitution of a basic group to fluorescent molecules. Following this concept, further studies would provide more sophisticated stimuli-responsive crystals, which should promote the practical application of luminescent smart crystals to sensing technologies.

Experimental

General

All air-sensitive experiments were carried out under an argon atmosphere unless otherwise noted. Silica gel 60 N (spherical, neutral, 63–210 μm) was used for column chromatography. 7-Bromobenzo[*c*][1,2,5]thiadiazole-4-carbaldehyde was synthesized according to the literature procedure.[10] Other reagents and solvents were commercially available and were used as received. ^{1}H and ^{13}C

NMR spectra were recorded on a JEOL ECA-500 spectrometer using tetramethylsilane as an internal standard. Elemental analyses were carried out on an Elementar UNICUBE elemental analyzer. A miniature fiber-optic spectrometer (FLAME-S-XR1-ES, Ocean Optics) and a LED light (365 nm, LSM-365A, Ocean Optics) were used for the measurements of fluorescence spectra of stimuli-responsive luminescence. Fluorescence and UV-vis absorption spectra were measured on a JASCO FP-8300 fluorescence spectrometer. The absolute fluorescence quantum yields (Φ_F) were determined using a 100 mm ϕ integrating sphere JASCO ILF-835. A KBr plate sample holder was used for the measurement of Φ_F to set a powdered sample between two KBr plates (5 × 5 × 1 mm). The solid-state absorption spectra were obtained by measuring diffuse reflectance spectra using an FPA-810 powder sample cell block. PXRD measurements were performed on a Rigaku SmartLab system using CuKα radiation. Melting points were determined on a Stuart melting point apparatus SMP3 and are uncorrected. DSC data were recorded on a Shimadzu DSC-60 plus (heating rate: 10 °C min^{-1}). XPS measurements were performed on a ULVAC-PHI Quantera SXM photoelectron spectrometer analyzer with a monochromatic Al Kα X-ray source. High-resolution mass spectra (HRMS-ESI) were recorded on a Hitachi Nano Frontier LD spectrometer.

Preparation of phenanthroimidazolylbenzothiadiazole derivatives

Synthesis of 4-bromo-7-[1-(4-methoxyphenyl)-1*H*-phenanthro[9,10-*d*]imidazol-2-yl]benzo[*c*][1,2,5]thiadiazole (2). To a solution of 7-bromobenzo[*c*][1,2,5]thiadiazole-4-carbaldehyde (248 mg, 1.0 mmol) and *p*-anisidine (189 mg, 1.5 mmol) in toluene (4.0 mL) were added 9,10-phenanthrenequinone (216 mg, 1.0 mmol) and ammonium acetate (475 mg, 6.1 mmol). After the mixture was stirred for 16 h at 120 °C, a saturated aqueous solution of $NaHCO_3$ and dichloromethane were added to the mixture. The organic layer was separated, and the aqueous layer was extracted three times with dichloromethane. The combined organic layer was washed with water and brine, dried over anhydrous Na_2SO_4, and filtered. After removal of the solvent under reduced pressure, the crude product was purified by column chromatography on silica gel (dichloromethane/toluene = 3 : 1) followed by recrystallization from hot toluene to give 4-bromo-7-[1-(4-methoxyphenyl)-1*H*-phenanthro[9,10-*d*]imidazol-2-yl]benzo[*c*][1,2,5]thiadiazole (**2**: 378 mg, 70%) as yellow crystals.

M.p. 244.0–244.2 °C; IR (ATR): ν_{max} 2998, 1509, 1453, 1245, 1021, 936, 877, 759, 727 cm^{-1}; ^{1}H NMR (500 MHz, $CDCl_3$): δ (ppm) 8.84–8.82 (m, 1H), 8.78 (d, *J* = 8.6 Hz, 1H), 8.71 (d, *J* = 7.9 Hz, 1H), 7.81–7.80 (m, 1H), 7.72–7.70 (m, 1H), 7.66–7.63 (m, 1H), 7.59–7.57 (m, 1H), 7.55–7.51 (m, 1H), 7.40–7.35 (m, 2H), 7.33–7.30 (m, 2H), 6.88–6.85 (m, 2H), 3.81 (s, 3H); ^{13}C NMR (126 MHz, $CDCl_3$): δ (ppm) 160.1, 153.27, 153.25, 147.4, 137.6, 132.4, 131.5, 130.1, 129.9 (2C), 129.5, 128.4, 128.3, 127.3, 127.2, 126.4, 125.8, 125.3, 124.1, 124.0, 123.1, 122.9, 122.8, 121.0, 115.8, 114.6 (2C), 55.5; HRMS-ESI (*m*/*z*): $[M+H]^+$ calcd for $C_{28}H_{18}BrN_4OS$, 537.0379; found, 537.0397.

Synthesis of 4-(4-methoxyphenyl)-7-[1-(4-methoxyphenyl)-1*H*-phenanthro[9,10-*d*]imidazol-2-yl]benzo[*c*][1,2,5]thiadiazole (1). A mixture of bromide **2** (242.1 mg, 0.45 mmol) and (4-methoxyphenyl)boronic acid (89.4 mg, 0.59 mmol) in a mixture of toluene (9.4 mL) and an aqueous solution of K_2CO_3 (1.0 mL, 1.4 M) was degassed under ultrasonication. $Pd(PPh_3)_4$ (34.9 mg, 0.03 mmol) was added to the mixture, which was further degassed under ultrasonication. After the mixture was stirred at 120 °C for 16 h, water and dichloromethane were added to the mixture. The organic layer was separated, and the aqueous layer was extracted three times with dichloromethane. The combined organic layer was washed with water and brine, dried over anhydrous Na_2SO_4, and filtered. After removal of the solvent under reduced pressure, the crude product was purified by column chromatography on silica gel (dichloromethane/toluene = 3 : 1) to give 4-(4-methoxyphenyl)-7-[1-(4-methoxyphenyl)-1*H*-phenanthro[9,10-*d*]imidazol-2-yl]benzo[*c*][1,2,5]thiadiazole (**1**: 219.2 mg, 86%) as a yellow solid.

M.p. 217.6–218.0 °C; IR (ATR): ν_{max} 2923, 1604, 1512, 1246, 1022, 796, 758, 728 cm^{-1}; ^{1}H NMR (500 MHz, $CDCl_3$): δ (ppm) 8.86 (dd, *J* = 7.9, 0.9 Hz, 1H), 8.80 (d, *J* = 8.8 Hz, 1H), 8.73 (d, *J* = 8.2 Hz, 1H), 7.93–7.91 (m, 2H), 7.77 (d, *J* = 7.3 Hz, 1H), 7.74–7.71 (m, 1H), 7.67–7.62 (m, 2H), 7.56–7.52 (m, 1H), 7.46–7.43 (m, 2H), 7.34–7.30 (m, 2H), 7.08–7.05 (m, 2H), 6.91–6.88 (m, 2H), 3.89 (s, 3H), 3.81 (s, 3H); ^{13}C NMR (126 MHz, $CDCl_3$): δ (ppm) 160.1, 160.0, 154.5, 153.4, 148.4, 137.6, 135.1, 132.4, 130.6 (2C), 130.5, 130.0 (2C), 129.4, 129.3, 128.30, 128.28, 127.31, 127.25, 126.3, 126.2, 125.6, 125.1, 124.1, 123.08, 123.05, 122.9, 122.5, 121.0, 114.5 (2C), 114.1 (2C), 55.4 (2C); HRMS-ESI (*m*/*z*): $[M+H]^+$ calcd for $C_{35}H_{25}N_4O_2S$, 564.1693; Found, 565.1702.

X-ray crystallography

Single crystals of **1•Toluene**, **1•Benzene**, **1•Pyridine**, **1•EtOAc**, and **1** were obtained by cooling hot solutions of **1** in toluene, benzene, pyridine, ethyl acetate, and *tert*-butylbenzene, respectively. A single crystal of **1•CHCl$_3$** was obtained from vapor diffusion of hexane into a chloroform solution of **1**. The crystalline samples were mounted on a glass fiber. All measurements were made on a Rigaku XtaLAB P200 diffractometer using multi-layer mirror monochromated Cu-Kα radiation (λ = 1.54184 Å). The data were collected at a temperature of –50 ± 1 °C. The crystal-to-detector distance was 40.00 mm. Readout was performed in the 0.172 mm pixel mode. Data were collected and processed using CrysAlisPro (Rigaku Oxford Diffraction).[11] An empirical absorption correction was applied. The data were corrected for Lorentz and polarization effects. All structures except **1•Benzene** were solved by direct methods (SHELXT Version 2014.4 or SIR92)[12] and expanded using Fourier techniques. The non-hydrogen atoms were refined anisotropically. Hydrogen atoms were refined using the riding model. All calculations were performed using the CrystalStructure[13] crystallographic software package except for refinement, which was performed using SHELXL Version 2014/7.[14] Using Olex2,[15] the structure of **1•Benzene** was solved with the SHELXT[16] structure solution program using Intrinsic Phasing and refined with the SHELXL[17] refinement package using Least Squares minimisation.

Crystal data for **1•Toluene** (CCDC2232778): $C_{42}H_{32}N_4O_2S$, *M* = 656.80, triclinic, *a* = 11.62224(9) Å, *b* = 14.66776(11) Å, *c* = 21.05256(16) Å, α = 100.6593(6)°, β = 91.6602(6)°, γ = 109.9863(7)°, *V* = 3297.98(5) Å^3, space group *P*-1 (no. 2), *Z* = 4, D_c = 1.323 g cm^{-3}, *F*(000) = 1376.00, *T* = 223(1) K, μ(Cu-Kα) = 12.212 cm^{-1}, 46430 reflections measured, 12036 independent (R_{int} = 0.0567). The final

refinement converged to R_1 = 0.0491 for $I > 2.0\sigma(I)$, wR_2 = 0.1400 for all data.

Crystal data for **1•CHCl$_3$** (CCDC2232779): $C_{36}H_{25}Cl_3N_4O_2S$, M = 684.04, monoclinic, a = 13.6322(2) Å, b = 22.3975(3) Å, c = 10.78060(19) Å, β = 111.601(2)°, V = 3060.44(9) Å^3, space group $P2_1/c$ (no. 14), Z = 4, D_c = 1.484 g cm^{-3}, F(000) = 1408.00, T = 223(1) K, μ(Cu-Kα) = 36.915 cm^{-1}, 18142 reflections measured, 5603 independent (R_{int} = 0.0580). The final refinement converged to R_1 = 0.0436 for $I > 2.0\sigma(I)$, wR_2 = 0.1252 for all data.

Crystal data for **1•Benzene** (CCDC2232780): $C_{41}H_{30}N_4O_2S$, M = 642.75, monoclinic, a = 27.8666(4) Å, b = 10.41560(10) Å, c = 23.2099(4) Å, β = 108.110(2)°, V = 6402.89(17) Å^3, space group $C2/c$ (no. 15), Z = 8, D_c = 1.334 g cm^{-3}, F(000) = 2688.0, T = 223(1) K, μ(Cu-Kα) = 12.46 cm^{-1}, 17502 reflections measured, 6248 independent (R_{int} = 0.0459). The final refinement converged to R_1 = 0.0533 for $I > 2.0\sigma(I)$, wR_2 = 0.1521 for all data.

Crystal data for **1•Pyridine** (CCDC2232781): $C_{40}H_{29}N_5O_2S$, M = 643.76, monoclinic, a = 27.6505(2) Å, b = 10.34767(8) Å, c = 23.2526(2) Å, β = 108.4906(10)°, V = 6309.54(9) Å^3, space group $C2/c$ (no. 15), Z = 8, D_c = 1.355 g cm^{-3}, F(000) = 2688.00, T = 223(1) K, μ(Cu-Kα) = 12.755 cm^{-1}, 19744 reflections measured, 5778 independent (R_{int} = 0.0247). The final refinement converged to R_1 = 0.0425 for $I > 2.0\sigma(I)$, wR_2 = 0.1145 for all data.

Crystal data for **1•EtOAc** (CCDC2232782): $C_{35}H_{24}N_4O_2S$, M = 564.66, monoclinic, a = 13.2848(2) Å, b = 21.9654(3) Å, c = 10.92692(17) Å, β = 111.8702(18)°, V = 2959.06(8) Å^3, space group $P2_1/c$ (no. 14), Z = 4, D_c = 1.267 g cm^{-3}, F(000) = 1176.00, T = 223(1) K, μ(Cu-Kα) = 12.752 cm^{-1}, 18511 reflections measured, 5402 independent (R_{int} = 0.0288). The final refinement converged to R_1 = 0.0425 for $I > 2.0\sigma(I)$, wR_2 = 0.1106 for all data.

Crystal data for **1** (CCDC2232783): $C_{35}H_{24}N_4O_2S$, M = 564.66, triclinic, a = 12.20306(9) Å, b = 21.16656(17) Å, c = 22.98109(18) Å, α = 69.0121(7)°, β = 87.5755(6)°, γ = 87.6112(6)°, V = 5534.93(8) Å^3, space group P-1 (no. 2), Z = 8, D_c = 1.355 g cm^{-3}, F(000) = 2352.00, T = 223(1) K, μ(Cu-Kα) = 13.635 cm^{-1}, 73764 reflections measured, 20185 independent (R_{int} = 0.0323). The final refinement converged to R_1 =0.0608 for $I > 2.0\sigma(I)$, wR_2 = 0.1783 for all data.

Elemental analyses data of solvates

The inclusion of solvate molecules were confirmed by elemental analyses. Since the most solvate molecules were evaporated during the preparation of the samples for measurement, the amount of included solvates was variable.

1•Toluene: Anal. Calcd. For $C_{35}H_{24}N_4O_2S•0.65C_7H_8•0.85H_2O$: C, 74.24; H, 4.87; N, 8.76; S, 5.01. Found: C, 74.15; H, 4.61; N, 8.50; S, 4.81.

1•CHCl$_3$: Anal. Calcd. For $C_{35}H_{24}N_4O_2S•1.0CHCl_3$: C, 63.21; H, 3.68; N, 8.19; S, 4.69. Found: C, 62.96; H, 3.66; N, 8.18; S, 4.58.

1•Benzene: Anal. Calcd. For $C_{35}H_{24}N_4O_2S•0.82C_6H_6•0.52H_2O$: C, 75.14; H, 4.73; N, 8.78; S, 5.02. Found: C, 74.99; H, 4.53; N, 8.63; S, 4.82.

1•Pyridine: Anal. Calcd. For $C_{35}H_{24}N_4O_2S•0.85C_5H_5N•0.45H_2O$: C, 73.66; H, 4.59; N, 10.61; S, 5.01. Found: C, 73.55; H, 4.47; N, 10.69; S, 4.89.

1•EtOAc: Anal. Calcd. For $C_{35}H_{24}N_4O_2S•0.68C_4H_8O_2$: C, 72.54; H, 4.75; N, 8.97; S, 5.13. Found: C, 72.29; H, 4.51; N, 9.18; S, 5.08.

Measurement of stimuli-responsive emission

Experimental procedure for the MCL of 1•Benzene. Crystalline samples of **1•Benzene** on an agate mortar were manually ground by using an agate pestle. The emission spectrum of the ground sample was measured using a miniature fiber-optic spectrometer. Ground samples of **1•Benzene** on a slide glass was placed in a petri dish (O.D. × height: 100 mm × 15 mm). In the same petri dish, benzene (ca. 3 mL) in another petri dish (O.D. × height: 40 mm × 10 mm) was placed. The larger petri dish was covered with a lid. After standing for 30 min at room temperature, the change in emission spectrum was observed using a miniature fiber-optic spectrometer.

Experimental procedure for the MCL of 1. Crystalline samples of **1** placed on a slide glass were manually crushed into fine powders by using an agate pestle. The emission spectrum of the crushed sample was measured using a miniature fiber-optic spectrometer. Crushed samples of **1** on an agate mortar were manually ground by using an agate pestle. The emission spectrum of the ground sample was measured using a miniature fiber-optic spectrometer. The ground sample of **1** placed on a slide glass was heated on a hot plate at 160 °C. After the heated sample was cooled to room temperature, the emission spectrum of the sample was measured using a miniature fiber-optic spectrometer.

Typical experimental procedure for the treatment of organic solvent vapors. Crystalline **1** on an agate mortar was manually ground by using an agate pestle. Ground **1** on a slide glass was placed in a petri dish (O.D. × height: 100 mm × 15 mm). In the same petri dish, organic solvent (ca. 3 mL) in another petri dish (O.D. × height: 40 mm × 10 mm) was placed. The larger petri dish was covered with a lid. After standing for 30 min at room temperature, the change in emission spectrum was observed using a miniature fiber-optic spectrometer.

Preparation of a mixture of 1 and pyridine hydrochloride. Crystalline **1** (23.2 mg, 0.041 mmol) and commercial pyridine hydrochloride (4.8 mg, 0.042 mmol) were dissolved in dichloromethane (10 mL). After removal of the solvent under reduced pressure, a mixture of **1** and pyridine hydrochloride was obtained as an orange solid. The mixture was placed on an agate mortar and was manually ground by using an agate pestle. The emission spectrum of the ground mixture was measured using a miniature fiber-optic spectrometer.

Theoretical calculations

The theoretical calculations were performed using the Gaussian 16 program.[18] An optimization of the molecular structures of **1** was carried out by DFT calculations at the CAM-B3LYP/6-31G(d) level of theory, using the single-crystal X-ray diffraction structures of solvates and solvate-free crystals of **1** as the initial geometry. The six lowest singlet–singlet transitions of the optimized structures of **1** were calculated using TD-DFT calculations at the CAM-B3LYP/6-31G(d) level of theory. Here, the long-range-corrected hybrid functional CAM-B3LYP was used, as CAM-B3LYP often provides better results in TD-DFT calculations than B3LYP, which is conventionally used in DFT calculations.[19] The results of theoretical calculations are presented in Table S2.

Fluorescence microscopy

Spatially resolved fluorescence measurements were performed on a home-built wide-field/confocal microscope equipped with a Nikon Ti-E inverted fluorescence microscope. The fluorescence images were recorded using a color sCMOS camera (Dhyana 400DC, Tucsen Photonics). The 405-nm continuous wave laser (OBIS 405LX, Coherent) or 405-nm pulsed diode laser (PiL040X, Advanced Laser Diode System, 45-ps FWHM) was used to excite the samples. A dichroic mirror (Di02-R405, Semrock) and a longpass filter (ET425lp, Chroma) were used to filter the scattering from excitation light. An area of approximately 1 μm^2 on a target particle or region was spatially selected using a 100-μm pinhole to measure its spectrum and fluorescence lifetime. For the spectroscopy, only the emission that passed through the pinhole and a slit entered the imaging spectrograph (MS3504i, SOL instruments) equipped with a CCD camera (DU416A-LDC-DD, Andor). For time-resolved fluorescence measurements, the emitted photons were passed through the pinhole and then directed onto a single-photon avalanche diode (SPD-050, Micro Photon Devices). The signals from the detector were sent to a time-correlated single photon counting module (SPC-130EM, Becker & Hickl) for further analysis. To separate the fluorescence signals, a bandpass filter (FF01-512/25, Semrock) was used. The instrument response function of the system was about 100 ps. All the experiments were conducted at room temperature. The data were analyzed using ImageJ (http://rsb.info.nih.gov/ij/) and Origin 2021 (OriginLab).

Author Contributions

Takumi Yagi: investigation, validation, visualization, writing – original draft. Takashi Tachikawa: conceptualization, funding acquisition, investigation, validation, writing – review & editing. Suguru Ito: conceptualization, funding acquisition, project administration, visualization, writing – review & editing.

Conflicts of interest

There are no conflicts to declare.

Acknowledgements

The authors are grateful to Mr. Shinji Ishihara and Ms. Yuko Kaneda (Instrumental Analysis Center, Yokohama National University) for their technical assistance in the elemental analyses and XPS measurements, respectively. This work was partly supported by JSPS KAKENHI Grant Number JP20K05645 within a Grant-in-Aid for Scientific Research (C), JSPS KAKENHI Grant Numbers JP20H04665 and JP20H04673 within a Grant-in-Aid for Scientific Research on Innovative Areas (“Soft Crystals: Area No. 2903”), and JST, PRESTO Grant Number JPMJPR21A3, Japan. Part of this work was carried out by the joint research program No. R04004 of Molecular Photoscience Research Center, Kobe University.

Notes and references

1 For reviews, see: (a) P. Gayathri, M. Pannipara, A. G. Al-Sehemi and S. P. Anthony, *CrystEngComm*, 2021, **23**, 3771; (b) E. Li, K. Jie, M. Liu, X. Sheng, W. Zhu and F. Huang, *Chem. Soc. Rev.*, 2020, **49**, 1517; (c) M. Kato, H. Ito, M. Hasegawa and K. Ishii, *Chem. Eur. J.*, 2019, **25**, 5105.

2 For reviews, see: (a) S. Ito, *J. Photochem. Photobiol.*, C, 2022, **51**, 100481; (b) T. Mutai and S. Takamizawa, *J. Photochem. Photobiol.*, C, 2022, **51**, 100479; (c) M. Jin and H. Ito, *J. Photochem. Photobiol.*, C, 2022, **51**, 100478; (d) S. Ito, *Chem. Lett.*, 2021, **50**, 649; (e) C. Wang and Z. Li, *Mater. Chem. Front.*, 2017, **1**, 2174; (f) Y. Sagara, S. Yamane, M. Mitani, C. Weder and T. Kato, *Adv. Mater.*, 2016, **28**, 1073; (g) Z. Ma, Z. Wang, M. Teng, Z. Xu and X. Jia, *ChemPhysChem*, 2015, **16**, 1811.

3 (a) Y. Sagara, K. Takahashi, A. Seki, T. Muramatsu, T. Nakamura and N. Tamaoki, *J. Mater. Chem. C*, 2021, **9**, 1671; (b) C. Duan, Y. Zhou, G. G. Shan, Y. Chen, W. Zhao, D. Yuan, L. Zeng, X. Huang and G. Niu, *J. Mater. Chem. C*, 2019, **7**, 3471; (c) S. Ito, G. Katada, T. Taguchi, I. Kawamura, T. Ubukata and M. Asami, *CrystEngComm*, 2019, **21**, 53; (d) Y. Takeda, T. Kaihara, M. Okazaki, H. Higginbotham, P. Data, N. Tohnai and S. Minakata, *Chem. Commun.*, 2018, **54**, 6847; (e) X. Wu, J. Guo, Y. Cao, J. Zhao, W. Jia, Y. Chen and D. Jia, *Chem. Sci.*, 2018, **9**, 5270; (f) S. Ito, T. Yamada and M. Asami, *ChemPlusChem*, 2016, **81**, 1272; (g) Z. Ma, Z. Wang, X. Meng, Z. Ma, Z. Xu, Y. Ma and X. Jia, *Angew. Chem., Int. Ed.*, 2016, **55**, 519; (h) Y. Matsunaga and J. S. Yang, *Angew. Chem., Int. Ed.*, 2015, **54**, 7985; (i) Y. Q. Dong, J. W. Y. Lam and B. Z. Tang, *J. Phys. Chem. Lett.*, 2015, **6**, 3429.

4 For a review, see: S. Ito, *CrystEngComm*, 2022, **24**, 1112.

5 (a) K. Zheng, F. Ni, Z. Chen, C. Zhong and C. Yang, *Angew. Chem., Int. Ed.*, 2020, **59**, 9972; (b) J. Y. Zhu, C. X. Li, P. Z. Chen, Z. Ma, B. Zou, L. Y. Niu, G. Cui and Q. Z. Yang, *Mater. Chem. Front.*, 2020, **4**, 176; (c) Y.-X. Li, Y.-G. Chen, Z.-F. Yu, X.-F. Yang, Y. Nie, Y. Cui and G.-X. Sun, *J. Phys. Chem. C*, 2020, **124**, 3784; (d) Z. Wang, M. Wang, J. Peng, Y. Xie, M. Liu, W. Gao, Y. Zhou, X. Huang and H. Wu, *J. Phys. Chem. C*, 2019, **123**, 27742; (e) Y. Wang, W. Liu, L. Ren and G. Ge, *Mater. Chem. Front.*, 2019, **3**, 1661; (f) T. Seki, T. Ozaki, T. Okura, K. Asakura, A. Sakon, H. Uekusa and H. Ito, *Chem. Sci.*, 2015, **6**, 2187.

6 (a) R. Yoshida, T. Tachikawa and S. Ito, *Chem. Commun.*, 2022, **58**, 6781; (b) R. Yoshida, T. Tachikawa and S. Ito, *Cryst. Growth Des.*, 2022, **22**, 547; (c) M. Yamashita, S. Nagai, S. Ito and T. Tachikawa, *J. Phys. Chem. Lett.*, 2021, **12**, 7826; (d) S. Ito, S. Nagai, T. Ubukata and T. Tachikawa, *CrystEngComm*, 2021, **23**, 5899; (e) S. Takahashi, S. Nagai, M. Asami and S. Ito, *Mater. Adv.*, 2020, **1**, 708; (f) S. Ito, S. Nagai, T. Ubukata, T. Ueno and H. Uekusa, *Cryst. Growth Des.*, 2020, **20**, 4443; (g) S. Ito, S. Nagai, T. Ubukata and M. Asami, *Chem. Lett.,* 2019, **48**, 1492; (h) S. Nagai, M. Yamashita, T. Tachikawa, T. Ubukata, M. Asami and S. Ito, *J. Mater. Chem. C*, 2019, **7**, 4988; (i) S. Ito, T. Taguchi, T. Yamada, T. Ubukata, Y. Yamaguchi and M. Asami, *RSC Adv.*, 2017, **7**, 16953; (j) S. Ito, T. Yamada, T. Taguchi, Y. Yamaguchi and M. Asami, *Chem. – Asian J.*, 2016, **11**, 1963.

7 For recent examples, see: (a) X. Han, X. Liu, N. Liu, W. Gao, Y. Lei, Y. Zhou, M. Liu, H. Wu and X. Huang, *J. Mater. Chem. C*, 2022, **10**, 9875; (b) R. Kubota, Y. Yuan, R. Yoshida, T. Tachikawa and S. Ito, *Mater. Adv.*, 2022, **3**, 5826; (b) Y. Liu, Z. Ma, J. Liu, M. Chen, Z. Ma and X. Jia, *Adv. Opt. Mater.*, 2021, **9**, 2001685; (c) J. Jia and L. Wu, *J. Photochem. Photobiol. A Chem.*, 2020, **399**, 112640; (d) S. Ito, C. Nishimoto and S. Nagai, *CrystEngComm*, 2019, **21**, 5699; (e) M. Kondo, T. Yamoto, S. Miura, M. Hashimoto, C. Kitamura and N. Kawatsuki, *Chem. - Asian J.*, 2019, **14**, 471; (f) B. Wang and C. Wei, *RSC Adv.*, 2018, **8**, 22806.
8 P. van der Sluis and A. L. Spek, *Acta Crystallogr., Sect. A: Found. Crystallogr.*, 1990, **46**, 194.
9 (a) E. V. Fedorenko, A. G. Mirochnik and A. A. Karpenko, *J. Photochem. Photobiol., A*, 2021, **420**, 113508; (b) J. Gierschner, S. Varghese and S. Y. Park, *Adv. Opt. Mater.*, 2016, **4**, 348.
10 J. Guo, S. Wang, N. Dai, Y. N. Teo and E. T. Kool, *Proc. Natl. Acad. Sci. USA*, 2011, **108**, 3493.
11 *CrysAlisPro: Data Collection and Processing Software*, Rigaku Corporation, Tokyo 196-8666, Japan, 2015.
12 (a) G. Sheldrick, *Acta Crystallogr.*, *Sect. A: Found. Crystallogr.*, 2014, **70**, C1437; (b) A. Altomare, G. Cascarano, C. Giacovazzo and A. Guagliardi, *J. Appl. Crystallogr.*, 1993, **26**, 343.
13 *CrystalStructure 4.2.5: Crystal Structure Analysis Package*, Rigaku Corporation, Tokyo 196-8666, Japan, 2000-2017.
14 G. M. Sheldrick, *Acta Crystallogr.*, *Sect. A: Found. Crystallogr.*, 2008, **64**, 112.
15 O.V. Dolomanov, L. J. Bourhis, R. J. Gildea, J. A. K. Howard and H. Puschmann, *J. Appl. Cryst.*, 2009, **42**, 339.
16 G. M. Sheldrick *Acta Crystallogr., Sect. A: Found. Crystallogr.*, 2015, **71**, 3.
17 G. M. Sheldrick *Acta Crystallogr., Sect. C: Struct. Chem.*, 2015, **71**, 3.
18 Gaussian 16, Revision A.03, M. J. Frisch, G. W. Trucks, H. B. Schlegel, G. E. Scuseria, M. A. Robb, J. R. Cheeseman, G. Scalmani, V. Barone, G. A. Petersson, H. Nakatsuji, X. Li, M. Caricato, A. V. Marenich, J. Bloino, B. G. Janesko, R. Gomperts, B. Mennucci, H. P. Hratchian, J. V. Ortiz, A. F. Izmaylov, J. L. Sonnenberg, D. Williams-Young, F. Ding, F. Lipparini, F. Egidi, J. Goings, B. Peng, A. Petrone, T. Henderson, D. Ranasinghe, V. G. Zakrzewski, J. Gao, N. Rega, G. Zheng, W. Liang, M. Hada, M. Ehara, K. Toyota, R. Fukuda, J. Hasegawa, M. Ishida, T. Nakajima, Y. Honda, O. Kitao, H. Nakai, T. Vreven, K. Throssell, J. A. Montgomery, Jr., J. E. Peralta, F. Ogliaro, M. J. Bearpark, J. J. Heyd, E. N. Brothers, K. N. Kudin, V. N. Staroverov, T. A. Keith, R. Kobayashi, J. Normand, K. Raghavachari, A. P. Rendell, J. C. Burant, S. S. Iyengar, J. Tomasi, M. Cossi, J. M. Millam, M. Klene, C. Adamo, R. Cammi, J. W. Ochterski, R. L. Martin, K. Morokuma, O. Farkas, J. B. Foresman and D. J. Fox, Gaussian, Inc., Wallingford CT, 2016.
19 D. Jacquemin, E. A. Perpète, G. E. Scuseria, I. Ciofini and C. Adamo, *J. Chem. Theory Comput.*, 2008, **4**, 123.